ACSNANO www.acsnano.org

ARTICLE

Protein-Assisted Assembly of Modular 3D Plasmonic Raspberry-like Core/Satellite Nanoclusters: Correlation of Structure and Optical Properties

Roland P. M. Höller,[†,‡] Martin Dulle,[§] Sabrina Thomä,[†] Martin Mayer,[‡] Anja Maria Steiner,[‡] Stephan Förster,[§] Andreas Fery,[†,‡,∥,⊥] Christian Kuttner,[*,†,‡,⊥] and Munish Chanana[*,†,#]

[†]Physical Chemistry II, University of Bayreuth, 95440 Bayreuth, Germany

[‡]Leibniz-Institut für Polymerforschung Dresden e.V., Institute of Physical Chemistry and Polymer Physics, Hohe Straße 6, 01069 Dresden, Germany

[§]Physical Chemistry I, University of Bayreuth, 95440 Bayreuth, Germany

[∥]Physical Chemistry of Polymeric Materials, Technische Universität Dresden, Hohe Straße 6, 01069 Dresden, Germany

[⊥]Cluster of Excellence Centre for Advancing Electronics Dresden (cfaed), Technische Universität Dresden, 01062 Dresden, Germany

[#]Institute of Building Materials, ETH Zürich, 8093 Zürich, Switzerland

Supporting Information

ABSTRACT: **We present a bottom-up assembly route for a large-scale organization of plasmonic nanoparticles (NPs) into three-dimensional (3D) modular assemblies with core/satellite structure. The protein-assisted assembly of small spherical gold or silver NPs with a hydrophilic protein shell (as satellites) onto larger metal NPs (as cores) offers high modularity in sizes and composition at high satellite coverage (close to the jamming limit). The resulting dispersions of metal/metal nanoclusters exhibit high colloidal stability and therefore allow for high concentrations and a precise characterization of the nanocluster architecture in dispersion by small-angle X-ray scattering (SAXS). Strong near-field coupling between the building blocks results in distinct regimes of dominant satellite-to-satellite and core-to-satellite coupling. High robustness against satellite disorder was proved by UV/vis diffuse reflectance (integrating sphere) measurements. Generalized multiparticle Mie theory (GMMT) simulations were employed to describe the electromagnetic coupling within the nanoclusters. The close correlation of structure and optical property allows for the rational design of core/satellite nanoclusters with tailored plasmonics and well-defined near-field enhancement, with perspectives for applications such as surface-enhanced spectroscopies.**

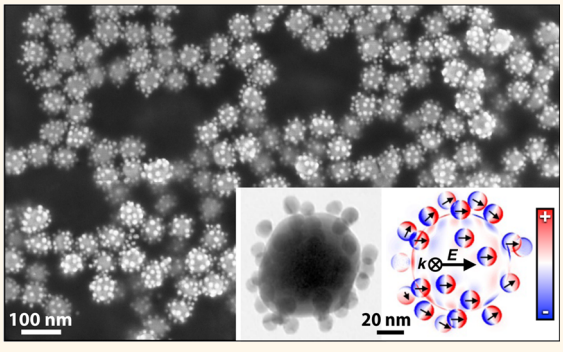

KEYWORDS: *protein-coated gold and silver nanoparticles, nanoparticle assembly, small-angle X-ray scattering (SAXS), plasmonic coupling, electromagnetic modeling, generalized multiparticle Mie theory (GMMT)*

Plasmonic core/satellite nanoclusters fabricated *via* self-assembly of subwavelength metal nanoparticles are highly interesting for their potential applications in the fields of optical metamaterials in particular optical sensing,[1,2] super-lensing (optical microscopy with super-resolution),[3,4] and cloaking (invisibility devices),[5,6] because these type of structures can support electric,[7,8] magnetic,[7,9] and even Fano-like resonances.[10−13] In addition, owed to the enhanced electromagnetic fields ("hotspots") between the NP building blocks and the resulting high surface plasmon resonance (SPR) sensitivity of these clusters, core/satellite nanoclusters are also highly promising for sensing applications such as surface-enhanced Raman spectroscopy (SERS) and SPR-shift-sensors,[14] respectively.

The predominant approaches to fabricate such raspberry-like core/satellite nanostructures are bottom-up strategies using

Received: November 29, 2015
Accepted: March 16, 2016
Published: March 16, 2016

DOI: 10.1021/acsnano.5b07533
ACS Nano 2016, 10, 5740−5750

organic (polystyrene,[15,16] viruses,[17,18] peptides,[19] *etc.*) or inorganic particles (SiO_2,[20−22] metals,[10,14,23−36] *etc.*) as cores and smaller inorganic nanoparticles such as gold, silver, or semiconductor NPs as satellites. In particular, in the case of (mere) metal/metal nanoclusters, organic linker molecules are usually employed to create a permanent link between the core and satellite particles.[37] The main classes of such organic linkers are (1) small α-ω end-functionalized molecular linkers[23−26] such as 1-9-nonanedithiol or *p*-aminothiophenol (*p*-ATP), (2) larger functionalized polymeric linkers,[10,14] (3) viruses,[27] and most prominently (4) linkers based on DNA base-pair interactions.[28−35] The DNA-assisted assembly method yields by far the best-defined nanocluster systems with precise structural order, relative geometry, and interparticle distances compared to other mentioned methods and, thus, represents the "gold standard" in terms of structural perfection. However, this method suffers from restrictions in terms of scalability because the resulting materials are restricted to low yields owed to the arduous and costly DNA engineering steps.

In most of the above-mentioned cases, the core−satellite assemblies are performed in dispersions without additional purification, *i.e.*, the isolation of nanoclusters.[10,14,26,29−33] General issues of the separation of the nanoclusters from the free building blocks are related to low yields, and inadequate colloidal stability to the harsh purification conditions.[25] Recently, isolated metal/metal core/satellite type assemblies have been achieved on solid substrates *via* sequential adsorption of NPs and α-ω functionalized linker molecules.[23−25,28] However, these structures are immobilized to solid supports and thus restricted in their properties and applications. Although in some cases core/satellite nanoassemblies[25] can be released from the support to form stable dispersions of asymmetric core/satellite structures, they may also suffer from low yields and undefined plasmonic properties. To the best of our knowledge, a simple method for producing three-dimensional (3D) metal/metal plasmonic nanoclusters in large-scale quantities and concentrations with tunable plasmonic properties and high colloidal stability and purity in solution has not been reported so far.

In this work, we present a simple and novel protein-assisted assembly process for the fabrication of metal/metal 3D core/satellite nanoclusters self-assembled in solution (Figure 1). This approach is highly modular in respect to size and the composition of the building blocks in combination with high satellite coverage close to the jamming limit. In addition, this method allows for the large-scale fabrication of plasmonic clusters with tunable optical properties. Such nanoclusters exhibit extraordinary optical properties due to plasmonic near-field coupling between the core and satellite NPs. To the best of our knowledge, this is the first small-angle X-ray scattering (SAXS) study of such metal/metal core/satellite nanoclusters. To reveal precise structural information, a suitable three-dimensional model including strong particle correlations (close to jamming limit) needed to be developed. We combine the results from SAXS, UV/vis spectroscopy, and electromagnetic simulations to correlate the structural parameters with the plasmonic coupling within core/satellite architectures. The fundamental understanding of metallic core/satellite assemblies reveals their potential for tailored plasmonics in the fields of surface-enhanced spectroscopy and design of magneto-optical metamaterials.[38]

RESULTS AND DISCUSSIONS

Protein-Assisted Self-Assembly of Nanoclusters. The approach for the synthesis of 3D plasmonic core/satellite nanoclusters *via* protein-assisted self-assembly is based on the

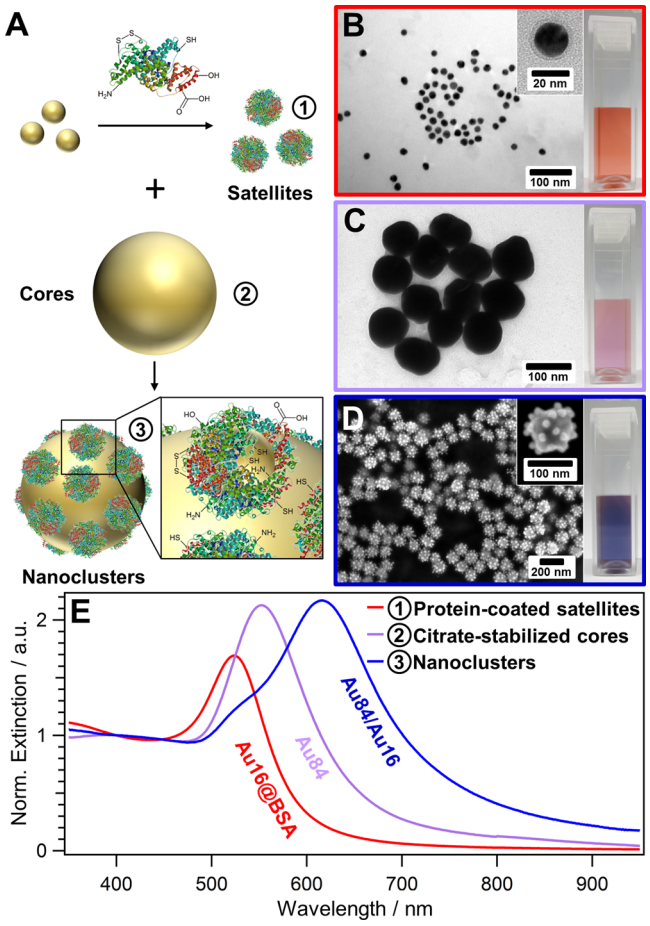

Figure 1. Protein-assisted self-assembly of metal/metal core/satellite nanoclusters. (A) Schematic illustration: citrate-stabilized satellite NPs are first coated with a protein giving protein-coated satellite NPs (1), which are assembled onto larger citrate-stabilized core NPs (2) yielding plasmonic core/satellite nanoclusters (3). Electron micrographs of (B) 16 nm bovine serum albumin (BSA)-coated AuNPs satellites, (C) 84 nm citrate-stabilized AuNPs cores, (D) the resulting Au84/Au16 nanoclusters, and their respective (E) UV/vis spectra. The cuvettes (insets B−D) show the purified dispersions of the building blocks and the nanoclusters.

physisorption of proteins to the particles in combination with their high binding affinities to metals.[39−46] The proteins act as an adhesive layer between the core and the satellite particles. Hence, in order to achieve a self-assembly of satellite NPs around the core NP, the satellite particles are first coated with a robust and homogeneous protein shell, as previously reported.[39−45] As depicted in Figure 1A, these colloidally stable protein-coated NPs bear sufficient functional groups such as thiols/disulfides, amines, and carboxylates to readily bind (unspecifically) to the metal surface of the core NPs, resulting into metal−core/metal−satellite nanoclusters. Hereby, the surface chemistry of the core particle before the assembly process, *i.e.*, the original coating/stabilizing agent, is of paramount importance. There are three prerequisites that the original stabilizing agent has to fulfill in order to ensure a successful particle assembly: (1) it has to provide sufficient colloidal stability to the core particles to avoid aggregation during the assembly process; (2) it should bind weakly enough to the core particle surface in order to be replaced easily by the protein-coated satellite NPs; and (3) the interactions between the original coating molecules and proteins (protein coatings) should be low in order to ensure the colloidal

DOI: 10.1021/acsnano.5b07533
ACS Nano 2016, 10, 5740−5750

stability of the resulting core/satellite nanoclusters. In this context, low-molecular-weight stabilizing molecules such as citrate[39−41] and tannic acid[47] have proven to be ideal stabilizing agents for the nanoparticle building blocks. First, these molecules have relatively low molecular weights (lower than proteins) and bind weakly to the gold nanoparticle surface and thus can be easily replaced by large proteins.[39−41,47] Second, they exhibit a negative net charge and therefore do not interact with negatively charged proteins and protein coatings (*i.e.*, at pH values above the isoelectric point) as shown recently.[45]

Hence, in the present study, we employ spherical gold and silver NPs in the size range of 5−100 nm, synthesized *via* different synthesis methods, as reported elsewhere (see Experimental Section).[47−51] Smaller NPs, typically with sizes below 35 nm, were used as satellites and larger NPs served as cores.

Figure 1A shows the general self-assembly process for the formation of plasmonic core/satellite nanoclusters. For instance, employing building blocks such as 16 ± 2 nm satellite NPs (Figure 1B) and 84 ± 8 nm core NPs (Figure 1C) can form colloidally stable Au84/Au16 core/satellite nanoclusters (Figure 1D). The size and the structure of the nanoclusters and their building blocks were determined by SAXS analysis, which will be discussed later in detail (see Elucidation of Structural Composition). The 16 nm spherical citrate-stabilized gold NPs were synthesized using the well-known citrate reduction method,[49] and coated subsequently with BSA in a ligand-exchange process (Figure 1B, inset), yielding homogeneous protein coating on the nanoparticles, as reported elsewhere.[39−45] The choice of the protein used for satellite coating, which functions as the "glue" in the assembly, strongly influences the structure formation. We tested different proteins in an effort to generate nanoclusters with different satellite coverage and satellites-to-core spacing (see Supporting Information, Figures S1−S4). In this work, we focus on nanoclusters assembled with BSA because these structures turned out to be the most robust system for the correlation of structure and optical properties. The satellite NPs reveal their localized surface plasmon resonance (LSPR) at 519 nm for citrate-coated NPs (Figure S5B) and 524 nm after protein coating (Figure 1E, red solid curve). Importantly, the protein-coated satellite NPs are highly purified (no protein excess) and exhibit high colloidal stability. Therefore, they can be concentrated to high particle concentrations,[41,44] which is essential in this cluster formation process. The designated Au core particles with an LSPR at 552 nm (Figure 1E, violet solid curve), which are also stabilized by citrate, were synthesized using the citrate reduction-based seeded-growth method reported by Puntes *et al.*[50] Finally, for the self-assembly of the satellite NPs onto the core surface, the core NPs were incubated with an excess of protein-coated satellite NPs, with a core-to-satellite ratio of 1:1000 (core NPs/satellite NPs).

The high excess of satellite NPs not only minimizes interparticle bridging of core particles, yielding stable and individually dispersed nanoclusters, but also ensures high surface coverage of the cores. Owed to the high colloidal stability of the satellite NPs and of the final nanoclusters, their separation becomes possible, simply *via* centrifugation (Figure S6). After the removal of the satellite NPs, the dominant LSPR at 600−620 nm of the self-assembled nanoclusters becomes more pronounced (Figure 1E and Figure S6), which is only present in such core/satellite structures (see Figure S7 for the control experiment). This mode indicates strong core-to-satellite coupling, which will be discussed in detail in the section Fundamental Coupling Scenarios.

The final purified product consisted of a dark blue dispersion (Figure 1D, inset), containing individually dispersed core/satellite nanoclusters (Figure 1E, blue curve). The clusters were characterized *via* transmission (TEM, Figure S6C) and scanning electron microscopy (SEM, Figure 1D) and UV/vis spectroscopy (Figure 1E). The UV/vis spectra of nanoclusters revealed two plasmonic modes: (1) a dominant radiant mode at 615 nm (strong core-to-satellite coupling, weak satellite-to-satellite coupling), which is 91 nm (satellite) and 63 nm red-shifted (core) from the LSPRs of its building blocks (see Figure 1E); and (2) a less pronounced nonradiant mode (weak core-to-satellite coupling, strong satellite-to-satellite coupling), which appears as a shoulder on the left flank of spectrum between 520 and 540 nm. We will focus on the explanation and quantification of the radiant and nonradiant nature of these modes in the final section of this paper (see Fundamental Coupling Scenarios and Influence of Satellite Disorder).

For plasmonic nanostructures and assemblies, it is well-known that parameters such as particle size, shape, and composition determine the final optical properties of a plasmonic nanomaterial.[52,53] Particularly, in the case of assemblies of plasmonic particles, other parameters such as the interparticle distances and the relative geometry of the particles to each other can also have a huge impact on the final optical properties of assembled systems.[42,54,55] In the following, we demonstrate that the protein-assisted self-assembly approach is highly modular in terms of parameters such as size and composition (*i.e.*, the material) of the building blocks, allowing for variable intercombinations of different metal NPs (*e.g.*, gold and silver NPs of different sizes) as core or satellites. Thus, this method is simple, highly modular, and versatile, allowing for facile tuning of the optical properties of such plasmonic assemblies in a broad range of the visible spectrum simply by changing these parameters. The simplicity of the approach in terms of varying particle size and composition and their influence on the optical/plasmonic properties of the clusters is discussed in detail in next section.

Modularity in Size and Composition. The modularity of the protein-assisted assembly process in size and composition is shown in Figure 2. Homometallic Au-core/Au-satellite nanoclusters (Figure 2A−C) and heterometallic Au-core/Ag-satellite nanoclusters (Figure 2D) were formed utilizing citrate-stabilized 84 nm gold NPs with an LSPR at 552 nm (Figure 2A−C, bottom, violet solid curve) for all four nanocluster systems and BSA-coated satellite nanoparticles (see Figure S5). For the homometallic gold nanoclusters, satellite NPs of different sizes, namely 5 nm (Figure 2A), 16 nm (Figure 2B), and 32 nm (Figure 2C) were used. For the heterometallic Au-core/Ag-satellite nanoclusters, silver NPs of 21 nm in size were employed as satellites (Figure 2D).

The homometallic gold core/satellite nanoclusters exhibited a dominant LSPR (*i.e.*, the radiant mode) at different wavelengths, depending on the size of the satellite NPs; all red-shifted differently from the LSPRs of their building blocks. Furthermore, the nonradiant mode *i.e.*, the shoulder on the left flank of the spectra, was less pronounced for the smaller satellites (Figure 2A) and more strongly pronounced for the bigger satellite NPs (Figure 2B,C): For the smallest satellite NPs of 5 nm, the radiant mode of Au84/Au5 nanoclusters was located at 566 nm and the nonradiant mode was poorly pronounced (Figure 2A). With medium-sized satellite NPs of 16 nm, the radiant-mode of Au84/Au16 nanoclusters shifted to 615 nm and the nonradiant mode ranged between 520 and 550 nm (Figures 1E and 2B). For the large satellites of 32 nm, the radiant mode of Au84/Au32

DOI: 10.1021/acsnano.5b07533
ACS Nano 2016, 10, 5740−5750

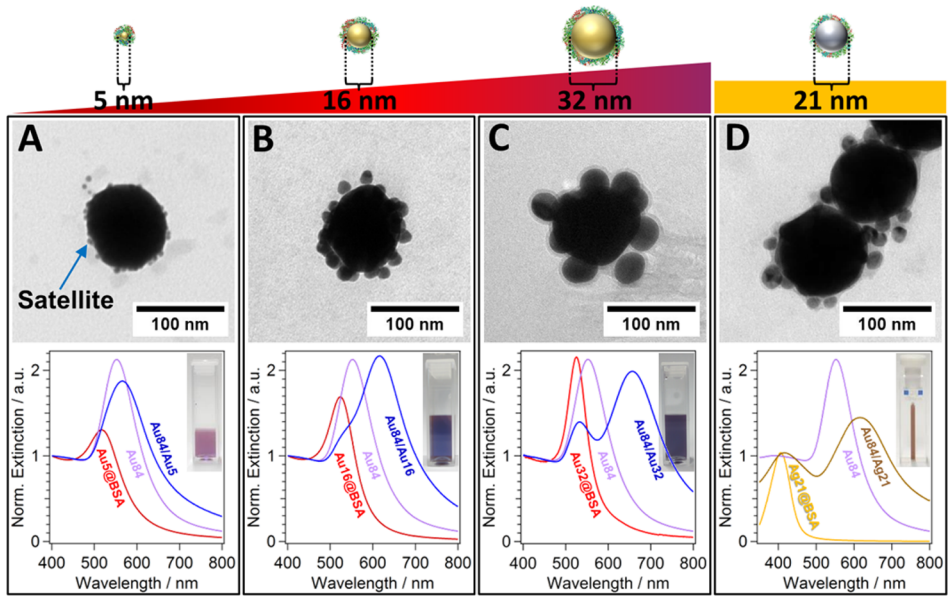

Figure 2. Modularity of nanoclusters in size and composition. TEM images (top) and UV/vis spectra (bottom) of homometallic and heterometallic core/satellite nanocluster dispersions (insets, bottom) with the same 84 nm-sized Au cores. BSA-coated Au satellites of increasing diameters (A) 5 nm, (B) 16 nm, and (C) 32 nm were used for the homometallic nanoclusters, showing the size modularity. BSA-coated Ag satellites of 21 nm in diameter were employed for the heterometallic nanoclusters (D), demonstrating the modularity of the assembly process in composition.

nanoclusters was located at 657 nm with a pronounced mode splitting and a separate nonradiant mode at 533 nm (Figure 2C). In general, one would expect a more pronounced redshift of the radiant mode for increasing satellite sizes. However, besides building block sizes also differences in core-to-satellite spacing and satellite coverage need to be taken into account. The radiant mode corresponds to core-to-satellite coupling, which will be discussed in detail in the section Fundamental Coupling Scenarios in the framework of plasmonic mode hybridization.

In the case of Au-core/Ag-satellite nanoclusters, 21 nm-sized silver satellites were synthesized using the sodium citrate/tannic acid reduction method for silver NPs reported by Puntes *et al.*[47] The as-synthesized silver satellite NPs exhibited their LSPR at 407 nm (Figure S5D) and at 406 nm after protein coating with BSA. For the self-assembly of heterometallic Au/Ag nanoclusters, an excess of protein-coated Ag satellite NPs was chosen, close to the ratio used for homometallic gold nanoclusters (see Experimental Section).

The final purified dispersions of the Au/Ag nanoclusters exhibited a pronounced brown color in transmission (Figure 2D, inset) and bluish color in reflectance (data not shown) in contrast to the dispersions of the individual building blocks. The Au/Ag nanoclusters also exhibited two distinct plasmonic modes. The first mode at 420 nm can be clearly attributed to the strong contribution of the Ag satellites. The second mode at higher wavelengths (617 nm) can be assigned to the strong coupling between the gold core particles and the silver satellite NPs. In comparison to homometallic gold nanoclusters (Au/Au), the splitting of the plasmonic modes of heterometallic nanoclusters (Au/Ag) is much more pronounced yielding two distinct LSPR bands (Figure 2D).

The optical response of core/satellite nanoclusters is sensitive to the size and the composition of the building blocks, the number of satellites (*i.e.*, surface coverage), the core-to-satellite separations, and the order/disorder in distribution of satellites. In the following, we will elucidate the structural composition of a selection of homometallic and heterometallic nanoclusters *via* SAXS measurements performed on their dispersions, in order to obtain the above-mentioned structural parameters for the various core/satellite nanoclusters (Figures 1 and 2).

Elucidation of Structural Composition: Nanocluster Morphology, Sizes, and Distances. SAXS represents a powerful tool for obtaining precise information on length scales from ~100 nm down to ~0.1 nm from samples in solution. In case of samples with low dispersity in size, very precise information on intra- and interparticle distances can be obtained by fitting the measured scattering curves with an appropriate model. The presented nanoclusters are especially well suited for such an investigation as their building blocks are scattering at very different q-values.

Figure 3 shows the exemplary characterization of the homometallic Au84/Au16 nanoclusters (compare Figure 1 and Figure 2B) with SAXS. The core with a radius of 42 nm has its first form factor minimum at a q-value of about 0.1 nm^{-1}, whereas the satellites have theirs at 0.6 nm^{-1}. The building blocks are all made of gold, which offers high and uniform contrast. As a result, the obtained scattering curves show distinct and well-pronounced features that allowed us to apply three-dimensional modeling to fit the SAXS data with a very low uncertainty. The applied model was based on 3D structures of nanoclusters with a disordered distribution of satellites following a random sequential adsorption (RSA) mechanism. The protein shell of BSA was not considered for the scattering as it has a negligible contrast compared to gold. Instead, the presence of the BSA shell was accounted for by the core-to-satellite distance. In the literature, an analytical model for Pickering-type emulsions is described,[56] which with a few modifications was easily applied to our data. However, this model cannot account for strong particle correlations. As our system is close to the jamming limit for randomly adsorbed particles on a surface, such particle correlations need to be taken into account. Thus, we chose to fit the

DOI: 10.1021/acsnano.5b07533
ACS Nano 2016, 10, 5740−5750

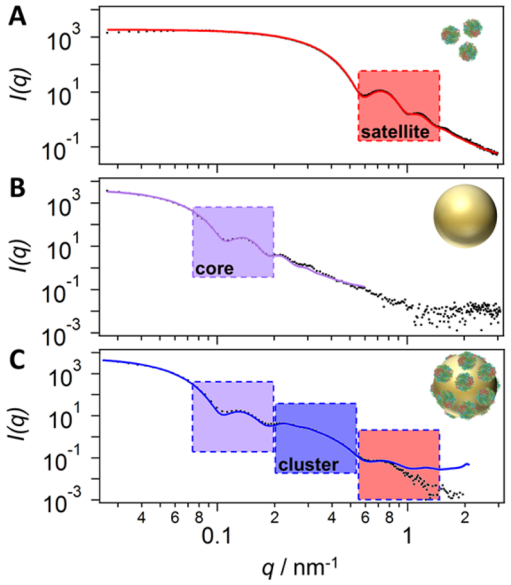

Figure 3. Characterization of the structural composition of core/satellite nanoclusters *via* small-angle X-ray scattering on the example of Au84/Au16 nanoclusters: (A) 16 nm BSA-coated satellite NPs, (B) 84 nm citrate-stabilized core NPs, and (C) the final Au84/Au16 core/satellite nanoclusters. The building blocks of the clusters were fitted with a model for polydisperse spheres (red and violet solid lines). The clusters were fitted with a three-dimensional core/satellite model based on the ensemble-averaged scattering of 10 individual randomly assembled nanoclusters (blue solid line, Table 1, column 1).

scattering data by directly calculating the ensemble-averaged scattering pattern of a large set of nanoclusters utilizing the formula of Debye.[57] The parameter space of core-to-satellite distance and surface coverage (number of satellites) was screened by a brute-force approach *i.e.*, calculating all possible combinations (in steps of 0.5% coverage and 0.1 nm distances) and judging their quality based on the corresponding mean squared error. Details on this approach as well as a comparison of the analytical model and the 3D-modeling approach can be found in the Supporting Information. To the best of our knowledge, this is the first small-angle X-ray scattering analysis of metallic core/satellite nanoclusters.

Using three-dimensional modeling, we were able to obtain structural parameters from the experimental data (see Figure 3). The sizes and the polydispersity of the building blocks were determined by fitting the respective scattering curves with SASview[58] and a simple model of polydisperse spheres (Figure S8A,B). Thus, only the coverage and the core-to-satellite distance needed to be varied (see Figures S8C and S9) for fitting the cluster data.

Table 1 shows the structural parameters for the nanoclusters assembled with BSA-coated satellites (for additional information see Figure S10). The first two columns show the results for the BSA-mediated homometallic Au84/Au16 and heterometallic Au84/Ag21 nanoclusters with a core size of 42 nm in radius. The best fit revealed an average coverage of 35 satellites for the homometallic clusters and 11 satellites for the heterometallic nanoclusters per core at an ensemble-averaged core-to-satellite distance of 4.3 and 4.0 nm, respectively. The core-to-satellite distance is most likely determined by the hydrated protein monolayer between the core and the satellite NPs. However, the 3D structure of the proteins between the core and the satellite NPs, which is hard to determine and yet unresolved, may differ

Table 1. Structural Composition of Different Nanoclusters with Different Building Block Sizes and Material Compositions As Characterized by SAXS

Radius of Au core NPs/nm[a]	42.0 ± 3.4	42.0 ± 3.4	35.3 ± 3.9
Satellite material	Au	Ag	Au
Radius of satellite NPs/nm[a]	7.5 ± 0.8	10.5 ± 1.2	7.2 ± 0.8
Satellite coating	BSA	BSA	BSA
Core-to-satellite distance/nm[b]	4.3 ± 0.3	4.0 ± 0.4	6.2 ± 0.5
Number of satellites per core[b]	35 ± 1	11 ± 1	23 ± 1
Corresponding Figures	2B	2D	S2D

[a]Variability in size is based on the standard deviation derived from a Gaussian distribution. [b]Variability in size of the satellites was omitted in the applied three-dimensional modeling of SAXS data. The given errors indicate the uncertainty of the ensemble-averaged core-to-satellite distance and number of satellites per core, respectively (see Supporting Information).

from the unassembled satellite NPs and the free protein in solution.

To show the size modularity of the core particle, we employed smaller NPs of 35.3 ± 3.9 nm radius and satellites of 7.2 ± 0.8 nm radius (Table 1, column 3 and Figure S2D). Remarkably, the core-to-satellite distances for the homometallic clusters with the smaller core ($R \approx 35$ nm) were found to be larger (*e.g.*, 6.2 ± 0.5 nm for BSA-mediated nanoclusters, Table 1, column 3) than the corresponding nanoclusters with the bigger core ($R \approx 42$ nm, Table 1, column 1). The reason why the core-to-satellite distances for the smaller core are larger is not clear yet. The environmental parameters, such as pH, ionic strength, temperature, and core-to-satellite ratio were kept constant for all assemblies. Nevertheless, the interparticle distances for all the clusters with the same core size lie consistently in the same range. A systematic SAXS study on tuning the interparticle distances within the nanoclusters accompanied by numerical and analytical modeling is the subject of ongoing work.

To correlate nanocluster structure and the optical response advanced modeling is required, addressing the fundamental coupling scenarios to evaluate the influence the structural changes on the optical properties. In the following, we will focus on one single nanocluster system to further quantify the effects of the structural composition on its electromagnetic characteristics. We have chosen the homometallic Au84/Au16 nanocluster with BSA-coated satellites because of the strong red shift of the radiant mode, pronounced mode splitting at high coverage of satellites, and the uniform X-ray scattering contrast of its building blocks.

Fundamental Coupling Scenarios. To elucidate the optical response of core/satellite nanoclusters, we first turn our attention to a model with a symmetric distribution and high coverage of satellites at the core surface (polygon model, see Figure S11). The two fundamental coupling scenarios can be described by a generalized hybridization model[59] (see Figures S12 and S13 for details).

As depicted in Figure 4A, both the single core and the orbit of satellites, for itself, form purely dipolar polarization states. When combined, two distinct modes arise in the extinction spectrum: a high-energy nonradiant mode with dominant absorption, and a low-energy radiant mode with dominant scattering. The nonradiant mode is shifted toward the blue below the excitation wavelength of the core. The electric field enhancement (Figure 4B) and the surface charge density (Figure 4C) show that the satellite-to-satellite coupling is dominant, while the satellite-to-core coupling is rather weak. Considering the difference in interparticle distances between the nanocluster

DOI: 10.1021/acsnano.5b07533
ACS Nano 2016, 10, 5740−5750

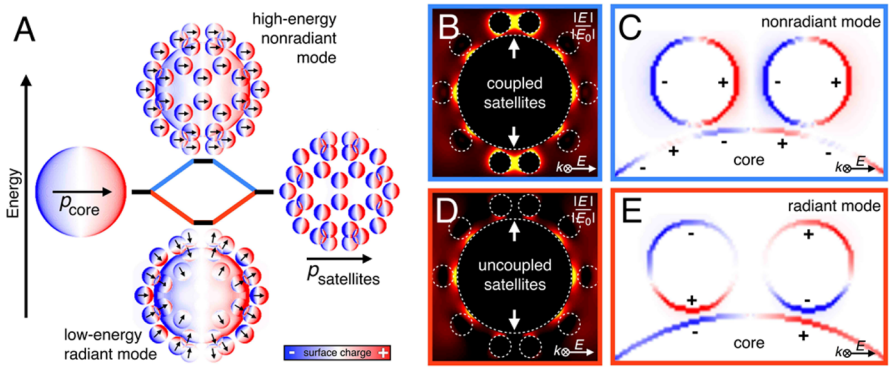

Figure 4. Polarization states of core/satellite clusters. (A) Main excitation states shown by surface charge densities with black arrows representing the orientation of the local dipole moments. (B) Electric field enhancement of the high-energy nonradiant mode with strong coupling between neighboring satellite particles (see white arrows). (C) Surface charges at the cross section of coupling satellites. (D) Electric field enhancement of the low-energy radiant mode showing no coupling between neighboring satellite particles. (E) Surface charges showing the dominant core-to-satellite coupling.

components in this model (core-to-satellite 4 nm; satellite-to-satellite 8 nm = 2× shell thickness of the protein layer in wet state) and the size ratio of the building blocks (diameter core/satellite = 84 nm/16 nm), one would expect the contrary. This can be explained by the antenna−receiver principle.[60] At lower wavelengths (compared to the core), the orbit of satellites acts as an antenna because the dipole moments of smaller particles are excited more easily by the present electric field. As a result, the core receives its polarization not from the external electric field but from the satellites ($p_{satellites}$), which can be clearly identified from the mirror charge patterns formed at the core surface (see Figure 4C). At higher wavelengths (compared to the core), the core acts as antenna and is directly polarized by the electric field (p_{core}). Consequently, the polarization of all satellites is oriented toward the core (see Figure 4A). For this low-energy radiant mode, satellite-to-satellite coupling is almost completely absent (Figure 4D). The dominant core-to-satellite coupling also results in a charge inversion of neighboring satellites at the meridian of the core (see Figure 4E). Thus, the two plasmonic modes shown in Figures 1 and 2 can be clearly attributed to the two principle coupling scenarios, as explained by this simple model of a nanocluster with a symmetric distribution and high coverage of satellites.

In the following, we address the close correlation of nanocluster structure and optical response to develop strategies for plasmonic tailoring.

Influence of Structural Changes on the Optical Response. To develop rational design criteria for core/satellite architectures, we first try to reproduce the experimental UV/vis spectrum of the Au84/Au16 nanoclusters using structural information determined by SAXS. The SAXS results for the sizes of the building blocks are in high accordance with values obtained from UV/vis spectroscopy and simple electromagnetic modeling (see Figure S14).

Figure 5A compares the experimental optical response of Au84/Au16 nanoclusters to modeled extinction spectra. The gray lines indicate the position of the measured radiant (λ_r) and nonradiant (λ_{nr}) modes. Although an ideally symmetric distribution of 30 satellites is quite close to the measured response, the experimental extinction curve (ratio and position of modes) cannot be described sufficiently without interpolation for variable numbers of satellites. To address this issue, we focus on the spectral shift of the dominant low-energy radiant mode. Figure 5B shows the correlation of the core-to-satellite distance

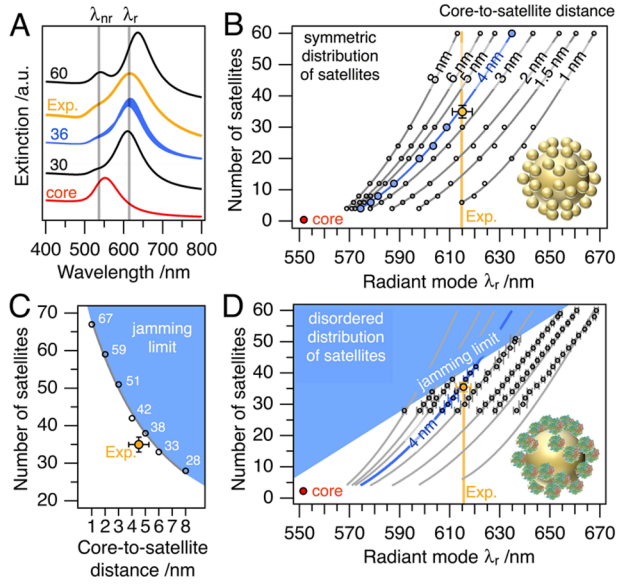

Figure 5. Correlation of nanocluster structure and optical response. (A) Measured Au84/Au16 sample (Exp., orange) and simulated optical response of core/satellite nanoclusters with different number of satellites per core at core-to-satellite separations of 4 nm (30 black, 36 blue, and 60 black line) and compared to an individual core particle (red line). The dominant radiant mode (λ_r) corresponds to the core-to-satellite coupling. Its spectral shift serves as a calibration from which the ensemble-averaged core-to-satellite distance and the number of satellites can be evaluated. The outstanding agreement of the (B) symmetric distribution and the (D) disordered distribution of satellites evidence the robustness of the optical response against disorder. In panels B and D, a 4 nm core-to-satellite distance (blue line) and 36 satellite particles agrees best with the experimental UV/vis data (Exp., orange). (C) The Au84/Au16 nanoclusters exhibit a high surface coverage close to the maximum number of satellite particles (jamming limit, blue area).

and the number of satellites. Considering only the measured extinction, neither the interparticle gaps nor the number of satellites can be determined. Taking into account the structural information from SAXS analysis, we find the best agreement for an Au84/Au16 nanocluster of 36 ± 2 satellites at a core-to-satellite distance of 4 ± 1 nm (see Table S1). The trend toward slightly shorter interparticle distances (compared to SAXS) may result from changes in refractive index caused by the

DOI: 10.1021/acsnano.5b07533
ACS Nano 2016, 10, 5740−5750

presence of the protein coating around the satellites (for details on refractive index sensitivity, see Figure S15). Tailoring of the nanocluster composition and morphology offers access to designed plasmonics in a broad range of wavelengths. However, the experimentally realized nanoclusters inherently possess asymmetric distributions of satellites owing to nonequidistant satellite-to-satellite distances (disorder) and the resulting steric limitations (jamming).

Influence of Satellite Disorder. In the following, we draw our attention toward disorder in satellite distribution. For this purpose, we applied a model taking a random sequential adsorption of satellite particles and the consequent coverage (jamming) limit into account. As shown in Figure 5A (blue line), a random distribution of 36 satellite particles closely reproduces the characteristics of the Au84/Au16 experimental data. Figure 5C shows the jamming limit with numbers of satellites given for various core-to-satellite distances. The Au84/Au16 nanoclusters are close to the maximum coverage expected for RSA-based assemblies. The deviation of the experimentally realized coverage from the theoretical prediction may indicate the presence of additional electrostatic repulsive interactions between satellite particles. The regime of inaccessible nanocluster compositions is also plotted in Figure 5D. Here, each data point represents 10 RSA-assembled clusters with the corresponding variances of the radiant modes plotted as error bars. The remarkable accordance of the predictions from the ideally symmetric clusters (gray regression lines in Figure 5B,D) and the randomly assembled clusters (RSA model; data points in Figure 5D) evidence the robustness of the optical response against satellite disorder, albeit for core-to-satellite distances at low surface coverages below 2 nm a distinct deviation toward lower wavelengths can be found. However, for the Au84/Au16 nanoclusters, the unperturbed coupling of satellites can be assumed.

To proof the robustness against disorder, *i.e.*, variations in satellite-to-satellite distances, we investigated the scattering and absorption contributions (losses) of the optical extinction. The strong agreement of experimental (Figure 6A) and modeled data (Figure 6B) clearly indicates the presence of two fundamental excitation regimes, each a prerequisite for distinct applications. The line width in Figure 6B represents the variance of the optical response based on 10 individual randomly assembled nanocluster configurations. Figure 6C,D shows the surface charge densities of an exemplary disordered Au84/Au16 nanocluster. At an excitation of 532 nm (see Figure 6C), the coupled satellites induce a mirror charge pattern at the core surface (green arrows, compare Figure 4C). At 633 nm, the dipolar excitation of the core is dominant. Consequently, all satellites are coupled to the core (see Figure 6D).

This proves that the two distinct coupling scenarios are unperturbed by disorder and their optical response is maintained (compare Figure 4A). Hence, ideally symmetric systems are not mandatory. Furthermore, the size of the core particle itself is a fundamental modality, for which a linear dependency was found regarding the spectral red shift of the radiant mode (see Figure S16). The high modality of the presented system may be exploited to gain control over the ratio of coupling between the building blocks, *e.g.*, the coupling between the satellites can be fully suppressed. This opens up possibilities for tailored nanoclusters with designed optical responses and "hotspot" locations. The latter would allow for spatial differentiation of the electric field enhancement, *i.e.*, predominantly between the satellites or exclusively in the gaps between core and satellites (compare Figure 4, panels B and D).

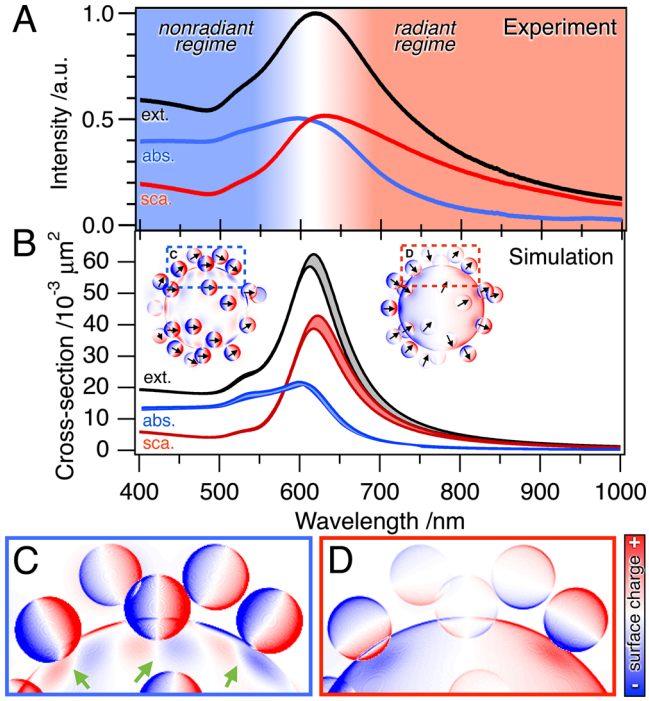

Figure 6. Nonradiant and radiant regimes of core/satellite nanoclusters. (A) Diffuse reflectance UV/vis spectroscopy measurements and (B) simulated absorption (blue line) and scattering contributions (red line) of the total extinction of Au84/Au16 (black line). Main excitation states shown by surface charge densities in the nonradiant and radiant regime (insets in B). The charge distribution of the core surface at (C) 532 nm mirrors the dominant intersatellite coupling (green arrows), whereas (D) at 633 nm, the dipolar excitation of the core and the resulting core-to-satellite coupling are dominant.

CONCLUSIONS

In conclusion, the protein-assisted self-assembly route presented in this work represents a powerful technique for the fabrication of three-dimensional colloidal nanoassemblies of plasmonic nanoparticles with core/satellite structure in dispersion. These plasmonic nanoclusters exhibit high colloidal stability and thus can be purified and concentrated to desired concentrations. The presented approach allows for tailoring on the nanoscale and provides access to colloidally stable and nanostructured plasmonic materials. In comparison to the assembly approaches reported in literature that use molecular linkers such as DNA or α-ω functionalized alkanes, or electrostatic interactions, the protein-assisted self-assembly method goes beyond the level of proof-of-principle and gives access to a readily available nanoassembled system.

The fabrication of stable nanoclusters was shown for homo- and heterometallic core/satellite combinations, with variable sizes of the building blocks, using bovine serum albumin. The protein serves as a multifunctional coating material, which acts as an adhesion layer, enabling cluster formation and as a soft spacer setting the core-to-satellite distances. The protein-coated satellites adsorb onto the core NP in a random sequential adsorption manner, leading to a disordered distribution of satellites on the core. Such core/satellite assemblies inherently exhibit two plasmonic modes based on distinct coupling regimes: (1) a nonradiant mode with dominant satellite-to-satellite coupling and (2) a radiant mode with dominant core-to-satellite coupling. Strikingly, the plasmonic coupling was found to be robust against

DOI: 10.1021/acsnano.5b07533
ACS Nano 2016, 10, 5740−5750

disorder. Thus, ideally symmetric assemblies are not mandatory. The structural parameters of the metallic core/satellite assemblies were studied in dispersion *via* small-angle X-ray scattering. For fitting the SAXS data, we developed an extended three-dimensional model based on the analytical model for Pickering emulsions,[56] taking strong particle correlations (close to the jamming limit) into account. The high modularity in sizes, composition, and satellite coverage enables precise optical and structural tailoring of three-dimensional nanoassemblies. Emerging fields such as subwavelength wave-guiding, photovoltaics, electric field enhancement, and metamaterials may benefit from the facile and readily up-scalable synthesis of designed nanoclusters. In particular, such plasmonic clusters open new avenues for biosensing applications based on SERS, exploiting biorecognition or guest−host interactions of proteins, which are intrinsically located right in the "hotspots".

EXPERIMENTAL SECTION

Materials. $HAuCl_4 \cdot 3H_2O$ (≥99.9%), $AgNO_3$ (99.9999%), sodium borohydride (99.99%), sodium citrate tribasic dihydrate (≥99%), tannic acid, bovine serum albumin (≥98%, BSA), cethyltrimethylammonium chloride solution (25 wt % in H_2O, CTAC), ascorbic acid (≥99%, AA), β-lactoglobulin from bovine milk (≥85%, BLG), conalbumin (CA) from chicken egg-white (substantially iron-free), recombinant human insulin and cytochrome *c* from bovine heart (≥95%, CYTC) were purchased from Sigma-Aldrich. Cethyltrimethylammonium bromide (≥99%, CTAB) was purchased from Merck KGaA. Sodium hydroxide concentrate (0.1 M, NaOH) was purchased from Grüssing GmbH. All chemicals were used as received. Milli-Q water was used in all experiments. All glassware was cleaned with *aqua regia* and rinsed extensively with Milli-Q water before use.

Synthesis of Citrate-Stabilized 5 nm AuNPs. Quasi-spherical citrate-stabilized AuNPs with an average particle size of ∼5 nm were synthesized by the borohydride reduction protocol reported by Jana *et al.*[48] A 20 mL aqueous solution containing 0.25 mM sodium citrate and 0.25 mM $HAuCl_4$ solution was prepared in a glass vial and thoroughly mixed. Then, 0.6 mL of a 0.1 M freshly prepared $NaBH_4$ solution was injected in one shot under vigorous stirring. After 2 min, the stirring was turned off and the solution was allowed to age for an additional 45 min. The final dispersion appeared brownish-red in color.

Synthesis of Citrate-Stabilized 16 nm AuNPs. Quasi-spherical citrate-stabilized AuNPs with an average particle size of ∼16 nm were synthesized by the citrate reduction method.[49] In a 1 L Erlenmeyer flask, 1.75 mL of a 0.1 M $HAuCl_4$ solution was added to 750 mL of Milli-Q water under stirring at room temperature and the solution was heated to boiling. Then, 18 mL of a 1 wt % sodium citrate solution was injected to the solution under vigorous stirring. The color of the solution changed from clear to blue, gray, and eventually reached its characteristic final wine-red color. The heating was stopped and the solution was allowed to cool to room temperature.

Synthesis of Surfactant-Stabilized 32 nm AuNPs. Spherical CTAC-stabilized AuNPs with an average particle size of ∼32 nm were synthesized by a seed-mediated growth method.[51] In a 15 mL glass vial, 300 μL of a freshly prepared aqueous solution of $NaBH_4$ (10 mM) was added to 4.7 mL of an aqueous solution containing $HAuCl_4$ (0.25 mM) and CTAB (100 mM) under vigorous stirring. After 2 min, stirring was reduced to a minimum and the CTAB-capped Au cluster seeds were aged for 20 min at 45 °C. Then, in a 100 mL glass vial, 40 mL of a 0.5 mM $HAuCl_4$ solution was added in one shot to a solution containing 40 mL of CTAC (200 mM), 3 mL of AA (1 M), and 460 μL of the aged CTAB-capped Au cluster seeds at 300 rpm. After 15 min, the resulting ∼10 nm Au seeds were centrifuged at 15 500 rcf for 20 min and washed with water. After the second centrifugation (15 500 rcf, 20 min), the AuNPs were redispersed in 10 mL of water for the following seed-mediated growth step. Therefore, in a 500 mL glass vial, 200 mL of a 1 mM $HAuCl_4$ in 50 mM CTAC solution was added dropwise (0.5 mL/min) to a solution containing 200 mL of CTAC (50 mM), 260 μL of AA (1 M), and 5 mL of the 10 nm Au seeds. After 15 min, the resulting 32 nm Au NPs were centrifuged at 12 000 rcf for 20 min and washed with water.

Seeded-Growth Synthesis of Citrate-Stabilized 71 and 84 nm AuNPs. Quasi-spherical citrate-stabilized AuNPs with an average particle size of ∼71 and ∼84 nm were synthesized by the citrate reduction-based seeded-growth method developed by Puntes *et al.*[50] In a 250 mL, three-neck round-bottom flask, 150 mL of a 2.2 mM aqueous solution of sodium citrate was heated in an oil bath for 15 min under reflux and vigorous stirring at permanent control of the solution temperature. At 100 °C, 1 mL of a 25 mM $HAuCl_4$ solution was immediately injected, by which the color of the solution changed from yellow to bluish gray and then to soft pink within 10 min. The resulting citrate-stabilized AuNPs were used as seeds for the next seeded-growth steps by successive addition of Au precursor, citrate solution, Milli-Q water, and dilution steps as reported elsewhere.[50] After 9 and 10 consecutive growth steps, the citrate-stabilized 71 and 84 nm AuNPs were obtained, respectively.

Synthesis of Citrate/Tannic Acid-Stabilized 21 nm AgNPs. Citrate/tannic acid-stabilized AgNPs with an average particle size of ∼21 nm were synthesized according to the sodium citrate/tannic acid reduction method, which was reported by Puntes *et al.*[47] In a 250 mL Erlenmeyer flask, 100 mL of an aqueous solution of sodium citrate (5 mM) and tannic acid (0.1 mM) was heated to boiling under permanent stirring. Immediately after boiling, 1 mL of an aqueous 25 mM $AgNO_3$ solution was injected under vigorous stirring. After the reaction was finished, the heating was stopped and the solution was allowed to cool to room temperature. The resulting AgNPs were purified (to remove the excess of tannic acid) by centrifugation (10 000 rpm, 30 min) and redispersed in an aqueous solution of 2.2 mM sodium citrate.

Protein-Coating of NPs *via* Ligand-Exchange. The citrate-stabilized or citrate/tannic acid stabilized satellite NPs were coated with different proteins (BSA, BLG, CYTC, and CA) using a simple ligand-exchange process that has been previously reported in the literature.[39−41,43] For AuNPs, the pH of the protein−citrate solution was adjusted to >9, for AgNPs to 9−9.5, respectively. For this, 90 mL of the citrate-stabilized NP dispersions was added dropwise to a 1 mg/mL protein/citrate solution under vigorous stirring. After 24 h at room temperature, the protein-coated NPs were purified (to remove excess protein) and concentrated by 5 centrifugation (8000−14 000 rpm, 0.5−4 h, depending on NP size) and redispersion cycles. The CTAC-stabilized satellite NPs were coated with BSA. Thirteen milliliters of the NP solution (CTAC concentration was set to 0.23 mM) was added to 30 mL of a 10 mg/mL BSA solution (pH 8) containing 0.02 wt % trisodium citrate under sonication. After 20 min sonication, the solution was centrifuged at 12 000 rcf for 1 h and the concentrated NPs were redispersed in one drop of a pH 11 NaOH solution and diluted with 30 mL of a 1 mg/mL BSA solution (pH 10) containing 0.02 wt % trisodium citrate. After incubation overnight at 4 °C, the functionalized NPs were washed 3 times at 12 000 rcf for 1 h with a pH 11.5 NaOH solution. The final dispersions were stored at pH ≥ 9 in a fridge.

Nanocluster Assembly. In a glass vial, 500 μL of citrate-stabilized core NPs (5×10^{10} NPs/mL) was added dropwise to 250 μL of highly purified and concentrated protein-coated satellite NPs (1×10^{14} NPs/mL). The pH of the satellite NP dispersion was adjusted to 10 before the core nanoparticles were added. After each addition step, the mixture was vortexed for 10 s. The nanoclusters were purified (to remove excess of satellite NPs) by 4 centrifugation (2000−3500 rpm, 5−12 min, depending on cluster size) and redispersion cycles. After each centrifugation step, the quality of the supernatant and the nanocluster dispersion were monitored *via* UV/vis spectroscopy. The final nanocluster dispersions were stored at pH ≥ 10 in a fridge.

Optical Characterization. UV/vis spectra were acquired with an UV/vis spectrophotometer SPECORD 250 PLUS (Analytik Jena AG). The extinction at the wavelength of 400 nm (interband transitions),[50] which is assumed to have a size-independent absorption coefficient,[61] was used to normalize the UV/vis spectra and to calculate the molar concentration of Au(0) in the NP dispersions. The molar concentration of Au(0) and the size of the nanoparticles obtained from TEM images

DOI: 10.1021/acsnano.5b07533
ACS Nano 2016, 10, 5740−5750

enabled the calculation of the particle concentration (number of AuNPs per volume). The absorption and scattering losses were determined using a UV/vis spectrophotometer Cary 5000 (Agilent Technologies Deutschland GmbH) equipped with the external diffuse reflectance accessory 2500 (integrating sphere). A quartz glass cuvette was positioned at the center of the integrating sphere and a fixed set of measurements was performed: sample measured without light trap; sample measured with light trap; and Milli-Q water measured without light trap as background. From this data, the absorption and scattering losses were calculated (see Supporting Information).

Electron Microscopy. TEM images were obtained using a TEM Zeiss CEM 902 (Carl Zeiss AG) with an accelerating voltage of 80 kV. SEM images were obtained using a SEM Zeiss 1530 (Carl Zeiss AG) equipped with a field-emission cathode with an operating voltage of 3 kV. Samples were prepared by spin-coating (2000 rpm, 30 s) of the NP dispersions on silicon wafers (Sigma-Aldrich), cleaned with Milli-Q water before use, and mounted on SEM aluminum pin stubs (Plano GmbH).

Small-Angle X-ray Scattering. SAXS experiments were performed with a "'Double Ganesha AIR" system (SAXSLAB, Denmark). The X-ray source of this laboratory-based system is a rotating anode (Cu, MicroMax 007HF, Rigaku Corporation, Japan) providing a microfocused beam at $\lambda = 0.154$ nm. The scattering data were recorded by a position-sensitive detector (PILATUS 300 K, Dectris). To cover the range of scattering vectors between 0.026 and 2 nm^{-1}, different detector positions were used. The measurements were done in 1 mm glass capillaries (Hilgenberg, code 4007610, Germany) at room temperature. The circularly averaged data were normalized to incident beam, sample thickness, and measurement time before subtraction of the solvent scattering curve.

Generalized Multiparticle Mie Theory Simulations. The optical responses of individual NPs as well as assemblies of NPs were modeled within the framework of the generalized multiparticle Mie theory (GMMT) based on analytic solutions for systems containing a finite number of ideally spherical particles.[62] For the GMMT calculations in this work, an algorithm developed by Yu-lin Xu[63,64] and Bo A. S. Gustafson[65] as well as the extension GMMFIELD by Moritz Ringler[66,67] were employed, using optical data by Johnson and Christy.[68] GMMT simulated extinction spectra of single gold spheres in water (refractive index $n = 1.333$) coincided with corresponding experimental data (see Figure S14). The presence of the protein coating was accounted for using a refractive index of $n = 1.395$. Consequently, GMMT was used for calculating the rotationally averaged extinction, absorption, and scattering cross sections of core/satellite assemblies. The original code by Yu-lin Xu was modified and extended to allow for parallelized calculations employing the btrzx3 linux cluster (70 cores @ 2.8 GHz with 4 GB RAM in total) at the University of Bayreuth. The high resource-efficiency of the optimized code allowed us to screen a variety of nanocluster configurations. The full ensemble of simulated spectra of nanoparticle assemblies (containing up to 61 particles at core-to-satellite distances ranging from 1 to 8 nm) with ideally symmetric and disordered satellite distributions were obtained within 14 days of total calculation time. Assemblies with ideally symmetric satellite distributions were modeled as Platonic and Archimedean polyhedra. Assemblies with disordered satellite distribution were modeled based on an algorithm following a random sequential adsorption mechanism. To account for the assembly variability, each morphological nanocluster species was represented by an ensemble calculated from ten randomly assembled configurations.

ASSOCIATED CONTENT

Supporting Information

The Supporting Information is available free of charge on the ACS Publications website at DOI: 10.1021/acsnano.5b07533.

Additional experimental data on the employed preparation methods and experimental procedures, satellites and nanoclusters of different protein coatings, long-term stability, nanocluster purification, SAXS modeling and analysis, optical characterization and GMMT modeling, reflective index sensitivity, influence of core size, diffuse reflectance UV/vis spectroscopy (PDF)

AUTHOR INFORMATION

Corresponding Authors

*E-mail: munish.chanana@uni-bayreuth.de.

*E-mail: christian.kuttner@ipfdd.de.

Notes

The authors declare no competing financial interest.

ACKNOWLEDGMENTS

The research leading to these results has received funding from the European Research Council under the European Union's Seventh Framework Programme (FP/2007-2013)/ERC Grant Agreement No. METAMECH-306686. We thank the IT service center at the University of Bayreuth (btrzx3 cluster) for computer resources. The authors further thank Bernd Kopera for help with programming of the polyhedra and the RSA mechanism, Dr. Tobias A. F. König, Dr. Thorsten Schumacher and Dr. Wolfgang Häfner for fruitful discussions, as well as Dr. Petr Formánek, Martina Heider and Carmen Kunert for electron microscopy measurements. This work benefited from SasView software, originally developed by the DANSE project under NSF award DMR-0520547 (http://www.sasview.org/help.html).

REFERENCES

(1) Liu, N.; Hentschel, M.; Weiss, T.; Alivisatos, A. P.; Giessen, H. Three-Dimensional Plasmon Rulers. *Science* **2011**, *332*, 1407−1410.

(2) Liu, N.; Weiss, T.; Mesch, M.; Langguth, L.; Eigenthaler, U.; Hirscher, M.; Sönnichsen, C.; Giessen, H. Planar Metamaterial Analogue of Electromagnetically Induced Transparency for Plasmonic Sensing. *Nano Lett.* **2010**, *10*, 1103−1107.

(3) Casse, B. D. F.; Lu, W. T.; Huang, Y. J.; Gultepe, E.; Menon, L.; Sridhar, S. Super-Resolution Imaging Using a Three-Dimensional Metamaterials Nanolens. *Appl. Phys. Lett.* **2010**, *96*, 023114.

(4) Rho, J.; Ye, Z.; Xiong, Y.; Yin, X.; Liu, Z.; Choi, H.; Bartal, G.; Zhang, X. Spherical Hyperlens for Two-Dimensional Sub-Diffractional Imaging at Visible Frequencies. *Nat. Commun.* **2010**, *1*, 143.

(5) Chen, P. Y.; Soric, J.; Alù, A. Invisibility and Cloaking Based on Scattering Cancellation. *Adv. Mater.* **2012**, *24*, OP281−OP304.

(6) Valentine, J.; Li, J.; Zentgraf, T.; Bartal, G.; Zhang, X. An Optical Cloak Made of Dielectrics. *Nat. Mater.* **2009**, *8*, 568−571.

(7) Simovski, C. R.; Tretyakov, S. A. Model of Isotropic Resonant Magnetism in the Visible Range Based on Core-Shell Clusters. *Phys. Rev. B: Condens. Matter Mater. Phys.* **2009**, *79*, 045111.

(8) Shalaev, V. M.; Cai, W.; Chettiar, U. K.; Yuan, H.-K.; Sarychev, A. K.; Drachev, V. P.; Kildishev, A. V. Negative Index of Refraction in Optical Metamaterials. *Opt. Lett.* **2005**, *30*, 3356−3358.

(9) Yen, T. J.; Padilla, W. J.; Fang, N.; Vier, D. C.; Smith, D. R.; Pendry, J. B.; Basov, D. N.; Zhang, X. Terahertz Magnetic Response from Artificial Materials. *Science* **2004**, *303*, 1494−1496.

(10) Fan, J. A.; Wu, C.; Bao, K.; Bao, J.; Bardhan, R.; Halas, N. J.; Manoharan, V. N.; Nordlander, P.; Shvets, G.; Capasso, F. Self-Assembled Plasmonic Nanoparticle Clusters. *Science* **2010**, *328*, 1135−1138.

(11) Ye, J.; Wen, F.; Sobhani, H.; Lassiter, J. B.; Dorpe, P. V.; Nordlander, P.; Halas, N. J. Plasmonic Nanoclusters: Near Field Properties of the Fano Resonance Interrogated with SERS. *Nano Lett.* **2012**, *12*, 1660−1667.

(12) Hentschel, M.; Dregely, D.; Vogelgesang, R.; Giessen, H.; Liu, N. Plasmonic Oligomers: The Role of Individual Particles in Collective Behavior. *ACS Nano* **2011**, *5*, 2042−2050.

(13) Lassiter, J. B.; Sobhani, H.; Fan, J. A.; Kundu, J.; Capasso, F.; Nordlander, P.; Halas, N. J. Fano Resonances in Plasmonic Nano-

DOI: 10.1021/acsnano.5b07533
ACS Nano 2016, 10, 5740−5750

clusters: Geometrical and Chemical Tunability. *Nano Lett.* **2010**, *10*, 3184−3189.
(14) Prasad, J.; Zins, I.; Branscheid, R.; Becker, J.; Koch, A. H. R.; Fytas, G.; Kolb, U.; Sönnichsen, C. Plasmonic Core−Satellite Assemblies as Highly Sensitive Refractive Index Sensors. *J. Phys. Chem. C* **2015**, *119*, 5577−5582.
(15) Qian, Z.; Hastings, S. P.; Li, C.; Edward, B.; McGinn, C. K.; Engheta, N.; Fakhraai, Z.; Park, S.-J. Raspberry-like Metamolecules Exhibiting Strong Magnetic Resonances. *ACS Nano* **2015**, *9*, 1263−1270.
(16) Sheikholeslami, S. N.; Alaeian, H.; Koh, A. L.; Dionne, J. A. A Metafluid Exhibiting Strong Optical Magnetism. *Nano Lett.* **2013**, *13*, 4137−4141.
(17) Lebedev, N.; Griva, I.; Dressick, W. J.; Phelps, J.; Johnson, J. E.; Meshcheriakova, Y.; Lomonossoff, G. P.; Soto, C. M. A Virus-Based Nanoplasmonic Structure as a Surface-Enhanced Raman Biosensor. *Biosens. Bioelectron.* **2016**, *77*, 306−314.
(18) Fontana, J.; Dressick, W. J.; Phelps, J.; Johnson, J. E.; Rendell, R. W.; Sampson, T.; Ratna, B. R.; Soto, C. M. Virus-Templated Plasmonic Nanoclusters with Icosahedral Symmetry *via* Directed Self-Assembly. *Small* **2014**, *10*, 3058−3063.
(19) Song, C.; Zhao, G.; Zhang, P.; Rosi, N. L. Expeditious Synthesis and Assembly of Sub-100 nm Hollow Spherical Gold Nanoparticle Superstructures. *J. Am. Chem. Soc.* **2010**, *132*, 14033−14035.
(20) Ponsinet, V.; Barois, P.; Gali, S. M.; Richetti, P.; Salmon, J. B.; Vallecchi, A.; Albani, M.; Le Beulze, A.; Gomez-Grana, S.; Duguet, E.; Mornet, S.; Treguer-Delapierre, M. Resonant Isotropic Optical Magnetism of Plasmonic Nanoclusters in Visible Light. *Phys. Rev. B: Condens. Matter Mater. Phys.* **2015**, *92*, 220414.
(21) Mühlig, S.; Cunningham, A.; Scheeler, S.; Pacholski, C.; Bürgi, T.; Rockstuhl, C.; Lederer, F. Self-Assembled Plasmonic Core−Shell Clusters with an Isotropic Magnetic Dipole Response in the Visible Range. *ACS Nano* **2011**, *5*, 6586−6592.
(22) Radziuk, D.; Schuetz, R.; Masic, A.; Moehwald, H. Chemical Imaging of Live Fibroblasts by SERS Effective Nanofilm. *Phys. Chem. Chem. Phys.* **2014**, *16*, 24621−24634.
(23) Ruan, Q.; Shao, L.; Shu, Y.; Wang, J.; Wu, H. Growth of Monodisperse Gold Nanospheres with Diameters from 20 to 220 nm and Their Core/Satellite Nanostructures. *Adv. Opt. Mater.* **2014**, *2*, 65−73.
(24) Cha, H.; Yoon, J. H.; Yoon, S. Probing Quantum Plasmon Coupling Using Gold Nanoparticle Dimers with Tunable Interparticle Distances Down to the Subnanometer Range. *ACS Nano* **2014**, *8*, 8554−8563.
(25) Yoon, J. H.; Lim, J.; Yoon, S. Controlled Assembly and Plasmonic Properties of Asymmetric Core−Satellite Nanoassemblies. *ACS Nano* **2012**, *6*, 7199−7208.
(26) Gandra, N.; Abbas, A.; Tian, L.; Singamaneni, S. Plasmonic Planet−Satellite Analogues: Hierarchical Self-Assembly of Gold Nanostructures. *Nano Lett.* **2012**, *12*, 2645−2651.
(27) Li, F.; Chen, H.; Zhang, Y.; Chen, Z.; Zhang, Z.-P.; Zhang, X.-E.; Wang, Q. Three-Dimensional Gold Nanoparticle Clusters with Tunable Cores Templated by a Viral Protein Scaffold. *Small* **2012**, *8*, 3832−3838.
(28) Zheng, Y.; Thai, T.; Reineck, P.; Qiu, L.; Guo, Y.; Bach, U. DNA-Directed Self-Assembly of Core-Satellite Plasmonic Nanostructures: A Highly Sensitive and Reproducible Near-IR SERS Sensor. *Adv. Funct. Mater.* **2013**, *23*, 1519−1526.
(29) Sebba, D. S.; Lazarides, A. A. Robust Detection of Plasmon Coupling in Core-Satellite Nanoassemblies Linked by DNA. *J. Phys. Chem. C* **2008**, *112*, 18331−18339.
(30) Sebba, D. S.; Mock, J. J.; Smith, D. R.; LaBean, T. H.; Lazarides, A. A. Reconfigurable Core−Satellite Nanoassemblies as Molecularly-Driven Plasmonic Switches. *Nano Lett.* **2008**, *8*, 1803−1808.
(31) Sebba, D. S.; LaBean, T. H.; Lazarides, A. A. Plasmon Coupling in Binary Metal Core−Satellite Assemblies. *Appl. Phys. B: Lasers Opt.* **2008**, *93*, 69−78.
(32) Millstone, J. E.; Georganopoulou, D. G.; Xu, X.; Wei, W.; Li, S.; Mirkin, C. A. DNA-Gold Triangular Nanoprism Conjugates. *Small* **2008**, *4*, 2176−2180.
(33) Maye, M. M.; Nykypanchuk, D.; Cuisinier, M.; van der Lelie, D.; Gang, O. Stepwise Surface Encoding for High-Throughput Assembly of Nanoclusters. *Nat. Mater.* **2009**, *8*, 388−391.
(34) Pal, S.; Sharma, J.; Yan, H.; Liu, Y. Stable Silver Nanoparticle-DNA Conjugates for Directed Self-Assembly of Core-Satellite Silver-Gold Nanoclusters. *Chem. Commun.* **2009**, 6059−6061.
(35) Wang, C.; Du, Y.; Wu, Q.; Xuan, S.; Zhou, J.; Song, J.; Shao, F.; Duan, H. Stimuli-Responsive Plasmonic Core-Satellite Assemblies: i-motif DNA Linker Enabled Intracellular pH Sensing. *Chem. Commun.* **2013**, *49*, 5739−5741.
(36) Choi, I.; Song, H. D.; Lee, S.; Yang, Y. I.; Kang, T.; Yi, J. Core−Satellites Assembly of Silver Nanoparticles on a Single Gold Nanoparticle *via* Metal Ion-Mediated Complex. *J. Am. Chem. Soc.* **2012**, *134*, 12083−12090.
(37) Kuttner, C.; Chanana, M.; Karg, M.; Fery, A. Macromolecular Decoration of Nanoparticles for Guiding Self-Assembly in 2D and 3D. In *Macromolecular Self-Assembly*; Billon, L., Borisov, O. V., Eds.; Wiley-VCH, 2016, in press, ISBN: 978-1118887127.
(38) Mayer, M.; Tebbe, M.; Kuttner, C.; Schnepf, M. J.; Koenig, T. A. F.; Fery, A. Template-Assisted Colloidal Self-Assembly of Macroscopic Magnetic Metasurfaces. *Faraday Discuss.* **2016**, DOI: 10.1039/C6FD00013D.
(39) Chanana, M.; Correa-Duarte, M. A.; Liz-Marzán, L. M. Insulin-Coated Gold Nanoparticles: A Plasmonic Device for Studying Metal−Protein Interactions. *Small* **2011**, *7*, 2650−2660.
(40) Strozyk, M. S.; Chanana, M.; Pastoriza-Santos, I.; Pérez-Juste, J.; Liz-Marzán, L. M. Protein/Polymer-Based Dual-Responsive Gold Nanoparticles with pH-Dependent Thermal Sensitivity. *Adv. Funct. Mater.* **2012**, *22*, 1436−1444.
(41) Chanana, M.; Rivera-Gil, P.; Correa-Duarte, M. A.; Liz-Marzán, L. M.; Parak, W. J. Physicochemical Properties of Protein-Coated Gold Nanoparticles in Biological Fluids and Cells before and after Proteolytic Digestion. *Angew. Chem., Int. Ed.* **2013**, *52*, 4179−4183.
(42) Hanske, C.; Tebbe, M.; Kuttner, C.; Bieber, V.; Tsukruk, V. V.; Chanana, M.; König, T. A. F.; Fery, A. Strongly Coupled Plasmonic Modes on Macroscopic Areas *via* Template-Assisted Colloidal Self-Assembly. *Nano Lett.* **2014**, *14*, 6863−6871.
(43) Tebbe, M.; Mayer, M.; Glatz, B. A.; Hanske, C.; Probst, P. T.; Müller, M. B.; Karg, M.; Chanana, M.; König, T. A. F.; Kuttner, C.; Fery, A. Optically Anisotropic Substrates *via* Wrinkle-Assisted Convective Assembly of Gold Nanorods on Macroscopic Areas. *Faraday Discuss.* **2015**, *181*, 243−260.
(44) Tebbe, M.; Kuttner, C.; Männel, M.; Fery, A.; Chanana, M. Colloidally Stable and Surfactant-Free Protein-Coated Gold Nanorods in Biological Media. *ACS Appl. Mater. Interfaces* **2015**, *7*, 5984−5991.
(45) Dewald, I.; Isakin, O.; Schubert, J.; Kraus, T.; Chanana, M. Protein Identity and Environmental Parameters Determine the Final Physico-Chemical Properties of Protein-Coated Metal Nanoparticles. *J. Phys. Chem. C* **2015**, *119*, 25482−25492.
(46) Moerz, S. T.; Kraegeloh, A.; Chanana, M.; Kraus, T. Formation Mechanism for Stable Hybrid Clusters of Proteins and Nanoparticles. *ACS Nano* **2015**, *9*, 6696−6705.
(47) Bastús, N. G.; Merkoçi, F.; Piella, J.; Puntes, V. Synthesis of Highly Monodisperse Citrate-Stabilized Silver Nanoparticles of up to 200 nm: Kinetic Control and Catalytic Properties. *Chem. Mater.* **2014**, *26*, 2836−2846.
(48) Jana, N. R.; Gearheart, L.; Murphy, C. J. Wet Chemical Synthesis of High Aspect Ratio Cylindrical Gold Nanorods. *J. Phys. Chem. B* **2001**, *105*, 4065−4067.
(49) Turkevich, J.; Stevenson, P. C.; Hillier, J. A Study of the Nucleation and Growth Processes in the Synthesis of Colloidal Gold. *Discuss. Faraday Soc.* **1951**, *11*, 55−75.
(50) Bastús, N. G.; Comenge, J.; Puntes, V. Kinetically Controlled Seeded Growth Synthesis of Citrate-Stabilized Gold Nanoparticles of up to 200 nm: Size Focusing *versus* Ostwald Ripening. *Langmuir* **2011**, *27*, 11098−11105.
(51) Zheng, Y.; Zhong, X.; Li, Z.; Xia, Y. Successive, Seed-Mediated Growth for the Synthesis of Single-Crystal Gold Nanospheres with

DOI: 10.1021/acsnano.5b07533
ACS Nano 2016, 10, 5740−5750

Uniform Diameters Controlled in the Range of 5−150 nm. *Part. Part. Syst. Charact.* **2014**, *31*, 266−273.
(52) Ross, M. B.; Ku, J. C.; Blaber, M. G.; Mirkin, C. A.; Schatz, G. C. Defect Tolerance and the Effect of Structural Inhomogeneity in Plasmonic DNA-Nanoparticle Superlattices. *Proc. Natl. Acad. Sci. U. S. A.* **2015**, *112*, 10292−10297.
(53) Ringe, E.; Van Duyne, R. P.; Marks, L. D. Correlated Structure-Optical Properties Studies of Plasmonic Nanoparticles. *J. Phys.: Conf. Ser.* **2014**, *522*, 012006.
(54) Barrow, S. J.; Wei, X.; Baldauf, J. S.; Funston, A. M.; Mulvaney, P. The Surface Plasmon Modes of Self-Assembled Gold Nanocrystals. *Nat. Commun.* **2012**, *3*, 1275.
(55) Funston, A. M.; Novo, C.; Davis, T. J.; Mulvaney, P. Plasmon Coupling of Gold Nanorods at Short Distances and in Different Geometries. *Nano Lett.* **2009**, *9*, 1651−1658.
(56) Larson-Smith, K.; Jackson, A.; Pozzo, D. C. Small Angle Scattering Model for Pickering Emulsions and Raspberry Particles. *J. Colloid Interface Sci.* **2010**, *343*, 36−41.
(57) Debye, P. Zerstreuung von Röntgenstrahlen. *Ann. Phys.* **1915**, *351*, 809−823.
(58) SasView, http://www.sasview.org/ (accessed Mar 1, 2016).
(59) Prodan, E.; Radloff, C.; Halas, N. J.; Nordlander, P. A Hybridization Model for the Plasmon Response of Complex Nanostructures. *Science* **2003**, *302*, 419−422.
(60) Tebbe, M.; Kuttner, C.; Mayer, M.; Maennel, M.; Pazos-Perez, N.; König, T. A. F.; Fery, A. Silver-Overgrowth-Induced Changes in Intrinsic Optical Properties of Gold Nanorods: From Noninvasive Monitoring of Growth Kinetics to Tailoring Internal Mirror Charges. *J. Phys. Chem. C* **2015**, *119*, 9513−9523.
(61) Rodríguez-Fernández, J.; Pérez-Juste, J.; Mulvaney, P.; Liz-Marzán, L. M. Spatially-Directed Oxidation of Gold Nanoparticles by Au(III)−CTAB Complexes. *J. Phys. Chem. B* **2005**, *109*, 14257−14261.
(62) Gouesbet, G.; Grehan, G. Generalized Lorenz-Mie Theory for Assemblies of Spheres and Aggregates. *J. Opt. A: Pure Appl. Opt.* **1999**, *1*, 706−712.
(63) Xu, Y.-l. Electromagnetic Scattering by an Aggregate of Spheres. *Appl. Opt.* **1995**, *34*, 4573−4588.
(64) Xu, Y.-l. Electromagnetic Scattering by an Aggregate of Spheres: Far Field. *Appl. Opt.* **1997**, *36*, 9496−9508.
(65) Xu, Y.-l.; Gustafson, B. Å. S. Comparison between Multisphere Light-Scattering Calculations: Rigorous Solution and Discrete-Dipole Approximation. *Astrophys. J.* **1999**, *513*, 894−909.
(66) Ringler, M. Plasmonische Nahfeldresonatoren aus zwei biokonjugierten Goldnanopartikeln. Ph.D. Thesis, Ludwig-Maximilians-University of Munich, 2008.
(67) Ringler, M.; Schwemer, A.; Wunderlich, M.; Nichtl, A.; Kürzinger, K.; Klar, T. A.; Feldmann, J. Shaping Emission Spectra of Fluorescent Molecules with Single Plasmonic Nanoresonators. *Phys. Rev. Lett.* **2008**, *100*, 203002.
(68) Johnson, P. B.; Christy, R.-W. Optical Constants of the Noble Metals. *Phys. Rev. B* **1972**, *6*, 4370−4379.

DOI: 10.1021/acsnano.5b07533
ACS Nano 2016, 10, 5740−5750